Remote Sens. **2014**, *6*, 11829-11851; doi:10.3390/rs61211829

OPEN ACCESS

remote sensing

ISSN 2072-4292

www.mdpi.com/journal/remotesensing

Article

Mineral Mapping and Ore Prospecting with HyMap Data over Eastern Tien Shan, Xinjiang Uyghur Autonomous Region

Hongyuan Huo [1,2], Zhuoya Ni [3,4], Xiaoguang Jiang [2,5,6], Ping Zhou [7] and Liang Liu [2,8]*

1 College of Urban and Environmental Sciences, Tianjin Normal University, Tianjin 300387, China; E-Mail: hongyuanh@gmail.com

2 College of Resources and Environment, University of Chinese Academy of Sciences, Beijing 100875, China; E-Mail: xgjiang@aoe.ac.cn

3 School of Geography, Beijing Normal University, Beijing 100875, China

4 ICube Lab, Université de Strasbourg, Centre National de la Recherche Scientifique, 67412 Illkirch, France; E-Mail: zni@unistra.fr

5 Key Laboratory of Quantitative Remote Sensing Information Technology, Academy of Opto-Electronics, CAS, Beijing 100094, China

6 Guilin University of Technology, Guilin 541004, China

7 China University of Geosciences, Beijing 100083, China; E-Mail: pxzhou@cugb.edu.cn

8 National Disaster Reduction Center of China, Ministry of Civil Affairs of the People's Republic of China, Beijing 100124, China

* Author to whom correspondence should be addressed; E-Mail: liuliang@ndrcc.gov.cn Tel.: +86-10-8825-6890.

External Editors: George P. Petropoulos and Prasad S. Thenkabail

Received: 15 September 2014; in revised form: 12 November 2014 / Accepted: 18 November 2014/ Published: 28 November 2014

Abstract: Using HyMap data, mineral identification and mineral mapping were conducted on the basis of the spectral absorption index (SAI) and other spectral absorption features in a study area in Tudun, eastern Tien Shan. Alteration minerals, such as calcite, alumina-rich (Al-rich) muscovite, epidote, and antigorite, were explored, and their relative abundance was depicted. A cross-validation was performed, and it showed a high degree of consistency between the imagery results and the results of previous literature. To further validate the mineral mapping from HyMap data, a field survey was carried out and rock samples were collected for quantitative analysis using a Por Infrared Mineral Analyzer (PIMA) and the software affiliated with it. Minerals were discriminated, and their relative abundance was

calculated from the spectra. Although we found that the absorption band-depth and SAI agreed well with each other and with the relative abundance of mineral alterations, the spectral absorption band-depth provided a better representation. Finally, ore prospecting of the study area was presented, and we found the distribution and close spatial relationships among the minerals extracted using the HyMap data. In the northern and northwestern part of the Gold-mine area, there was a mineralized muscovite alteration showing a sheet or block distribution. In the Copper-mine area, Al-poor muscovite with a sheet distribution was distributed in the north and northeast region, and Al-rich muscovite showed a block distribution enclosed by the distribution area of Al-poor muscovite. These all showed good ore prospects for the study area.

Keywords: HyMap; hyperspectral remote sensing; mineral mapping; spectral absorption features

1. Introduction

Optical remote sensing (RS) data are used for mineral exploration to (a) map geology and the faults and fractures that are associated with ore deposits and (b) recognize hydrothermally altered rocks on the base of their spectral signature. The visible and near infrared wavelengths and the shortwave infrared region are mostly used in geological applications according to much previous literature [1–8]. Thermal remote sensing is valuable for discriminating the Silicate minerals according to their different temperature, due to the different spectral channel and their respective spectral emittance variations [9–19], and the SAR data has also been successfully used in discriminating the Lithology of the rock according to their different Backscattering coefficients under the condition of different Polarization and Surface roughness [20,21].

Mineral identification is the core and foundation of the geological application of hyperspectral remote sensing [22–26]. The basic principle for quantitatively extracting mineral alterations with hyperspectral remote sensing is to make a quantitative and comparative analysis between a hyperspectral imagery spectrum and mineral spectra measured using laboratory/standard mineral spectroscopy. According to previous literature, the methods for mineral alteration identification based on absorption features can be classified into two types, including (a) the complex method based on the mineralogy and knowledge of diagnostic absorption features for mineral identification (more details can be found in [27]) and (b) the spectrum matching algorithm based on calculations of the similarity between the test spectrum and a reference spectrum (literature on measuring similarity function based on the whole spectrum has been developed by many scientists [28–37]).

Previous articles on mineral identification using the spectral matching method on the basis of local spectral absorption features such as absorption band-position, absorption band-depth, absorption symmetry and absorption band-width have been developed by many scientists [38–41]. Clark *et al.* [37] put forward the so-called Spectral Feature Fitting (SFF) method to match target and reference pixel spectra by examining specific absorption features in continuum-removed spectra. Júnior [38] presented an Analysis of Absorption Band Positioning (AAPB) method. The AAPB method is used to identify alteration minerals and map their corresponding abundance by calculating and generating an image

related to the pixel spectrum absorption band position. This method can be used as an exploratory stage and in the analysis refinement stage for its advantages in discriminating spectra with high similarity and proximity. Wang *et al.* (1996) [39] proposed a model named the Spectral Absorption Index (SAI) for extracting alteration mineral information. In fact, the SAI algorithm is a function related to the relative spectral band depth, minimizing the impacts of non-absorption material on the spectra through a non-absorbing baseline equation and a ratio method. Van Ruitenbeek, *et al.* (2006) [41] presented a method that uses the pixel-dependent information only and that is based on extracting diagnostic spectral information of the mineral of interest through band ratios to estimate the presence of white micas at the earth surface, and the results showed the predicted wavelengths of white mica in the areas of highest probability of containing white mica. The principal component analysis (PCA) and other supervised/unsupervised classification methods often also provide an ability to discriminate minerals using multi-spectral satellite data (e.g., Landsat Thematic Mapper (TM) data and Advanced Spaceborne Thermal Emission and Reflection Radiometer (ASTER) data) [42–45].

In spite of these significant contributions mentioned above, no substantial research in China has yet attempted to study mineral mapping based on spectral absorption features and an SAI model using the HyMap data, particularly to analyze the relationship between the abundance of minerals based on spectral absorption features and that based on the SAI model using a PIMA spectrometer. The objectives of this paper are (1) to map the abundance of alteration minerals using spectral absorption features and SAI based on prior knowledge of mineral spectra, (2) to analyze the relationship between mineral abundance (from spectra of test samples collected via field survey) and spectral absorption features and the SAI, and (3) mapping the potential ore deposits in the study area.

2. Geology of the Study Area

The study area is located in the Tudun area, southeast of Hami City and 20 kilometers from the city center, in Xinjiang Uyghur Autonomous Region, NW China (See Figure 1a). The study area is geographically divided into two parts (See Figure 1). The first area is the so-called Gold mine area, delimited by 94°4′–94°7′E； 42°12′–42°15′N, and the second area is the Copper mine area, delimited by 94°5′–94°11′E; 42°9′40″–42°13′N. The study area is located at the conjunction of the Tarim plate and the Junggar Plate, and it is a part of the Tage Kangguer Devonian and Carbo island arc belt in the southeast margin of the Junggar plate, and it is also a part of the Jueluotage Carboniferous island arc in the active leading edge of the Tarim plate. The outcrop formation is crystalline basement and cap formation. The metallogenic belt underwent multiple phases of deformation related to more intensive magmatic activity, the fractures and folds were well developed, producing various types and scales of polymetallic deposits with Mo, Cu, Ni, Fe as the main metallogenic elements [46]. The metamorphism in the study area is mainly dynamic metamorphism and hydrothermal metamorphism. The formation of dynamic metamorphism alterations in the area mainly accompany fault structures, and the corresponding distribution occurs in a zonal shape along the tectonic line. The formation of hydrothermal metamorphism is located in the fault structure belt and interlayer fracture. The hydrothermal alterations include altered stages of pyrite-sericitization, silicification, carbonation, epidotization, chloritization, sericitization, kaolinization, and potassic alteration accompanied by formations of pyrite, malachite, galena and gold [47]. The Tudun area in Hami City, in East Tien Shan mountain, in Xinjiang Uyghur

Autonomous Region, NW China, is a part of the central Asian grassland and desert region, thus, the study area has a continental climate with long, cold winters and very hot, dry summers; the average annual precipitation is 32 mm, there's no rivers and other larger water bodies, almost no vegetation covering this area.

Figure 1. Study area of Tudun gold-mine area and copper mine area (**a**). Location and direction of study area in northwest China (**b**). The study area located in Hami city, Xinjiang Uyghur Autonomous Region, and (**c**) is a false color composite image by R/G/B: 7/4/2 of Landsat ETM+ acquired on 12 July 2000 (c). Locations of the two major gold and copper mines in the Tudun area. Projection: UTM, zone 48 North, WGS 84.

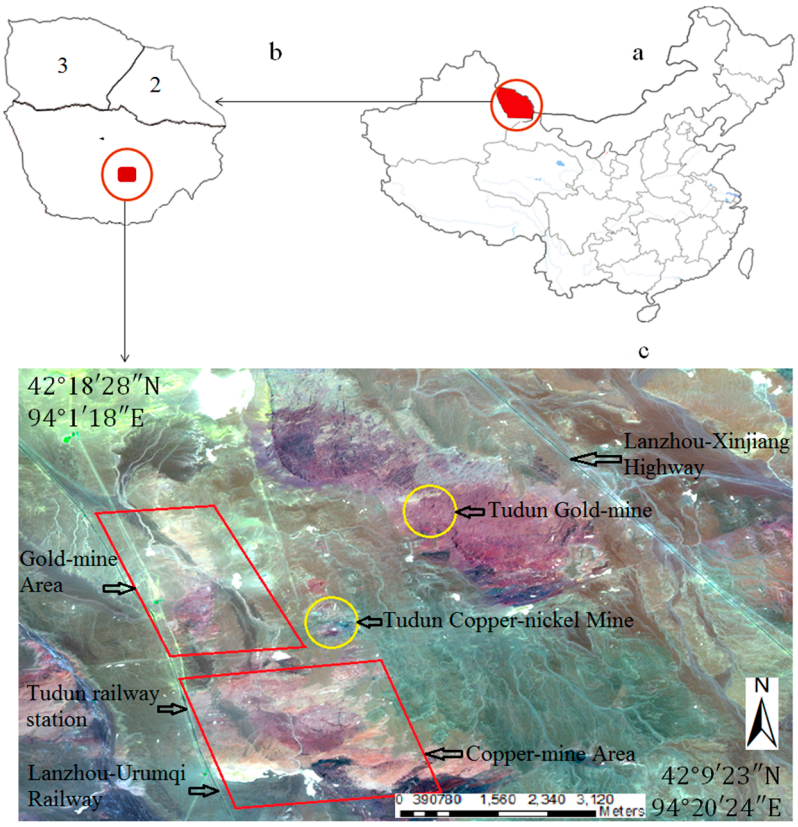

3. Data and Preprocessing

3.1. HyMap Dataset

The HyMap hyperspectral scanner (Manufactured by Integrated Spectronics Pty Ltd, Sydney, Australia) is operated by HyVista Corporation and weighs 200 kg. The spectral configuration of the HyMap sensor includes four spectral modules acquiring 32 bands each, totaling 128 spectral bands. The sensor operates in a tri-axis gyro stabilized platform to minimize image distortion due to aircraft motion. The system, integrated with the Global Position System (GPS) and an Inertia Monitoring Unit (IMU), can be rapidly adapted into any aircraft with a standard aerial camera port and is transported between international survey sites by air freight. Geolocation and image geocoding are achieved with DGPS and the integrated IMU. Laboratory calibration and operational system monitoring ensures that the imagery is calibrated as required for demanding spectral mapping tasks. The HyMap datasets used in the study are

Level 2 reflectance hyperspectral datasets that have been processed through radiometric calibration, geometric correction and atmospheric correction with the 6S model, totaling 122 bands without the six bands influenced by water vapor; the detailed technical parameters are listed in Table 1 [48]. A flowchart of the study is presented in Figure 2. The HyMap airborne data used in this study was captured on 24 October 2002 with a cloud-free day, in East Tien Shan Mountain, and there's almost no vegetation in the study area. The preprocessing of HyMap data occurred in several steps. The first was to convert the original Digital Number (DN) to radiance using the DN-to-radiance conversion factors that accompanied HyMap data. The next task was atmospheric correction. The atmospheric effects were removed by the HyCorr for HyMap Atmospheric Correction (HHAC) module. The HHAC module was developed by the HyVista Co. Ltd. (Sydney, Australia) on the basis of the Second Simulation of the Satellite Signal in the Solar Spectrum (6S) module. Then, the spectral reflectance of the captured HyMap data was rebuilt for the further analysis and the mineral mapping with the SAI.

Figure 2. Flowchart of the study.

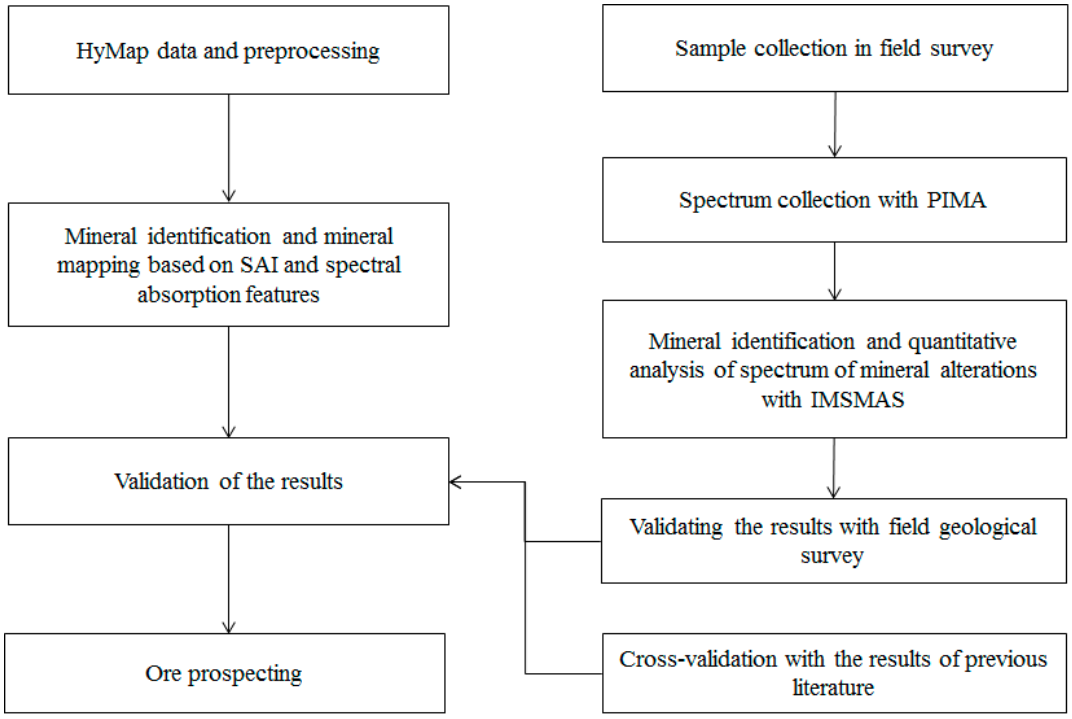

Table 1. Relevant technical parameters of the HyMap spectrometer [48].

Wavelength (nm)	Bandwidth (nm)	Average Spectral Sampling Interval (nm)	Band Number
VIS：450–890	15–16	15	32
NIR：890–1350	15–16	15	32
SWIR1：1400–1800	15–16	13	32
SWIR2：1950–2480	18–20	17	32
IFOV	2.5 mr along track, 2.0 mr across track		
GIFOV	3–10 m		
Data coding	16 bit		
SNR	>500:1		

3.2. PIMA

The Portable Infrared Mineral Analyzer (PIMA) used in the study, manufactured by Zhongdi Co. Ltd., Nanjing, China, is a spectrometer operated in laboratory/field surveys that works in the SWIR spectral region. The main technical parameters can be described as follows: the working spectral region ranges from 1300 nm to 2500 nm, the spectral resolution is 7 nm, the spectrum sampling interval is 2 nm, the signal to noise ratio (SNR) is 2500:1, and the average duration of a standard measurement is 37 seconds. The PIMA spectrometer has an advantage of low cost, lightweight, fast testing and no sample preparation. The test samples include rock, soil and water. Moreover, the spectrometer has a built-in light source, so light is not a factor and it can be used to carry out indoor/underground spectral testing. In addition, using the PIMA, different crystal forms of the same type of mineral can be distinguished.

4. Methods

4.1. Spectral Absorption Features of Main Alteration Minerals

The analysis of minerals using the near infrared (NIR) spectral region is an important tool for identifying and studying minerals and analyzing their components. Some parts of the infrared spectrum can be absorbed due to the bending and stretching of chemical bonds between atoms in a mineral crystal lattice. According to certain diagnostic spectral absorption features of molecular bonds, the mineral can be identified, and the degree of crystallinity of the mineral can be distinguished. These characteristics of minerals presented within the NIR spectral region are of great importance for geological field surveys. Based on the above-mentioned principle, we can discriminate single minerals from phyllosilicate (e.g., clay minerals, chlorite, antigorite), identify silicate minerals containing OH molecular bonds (e.g., epidote, amphibole), and sulfate minerals (e.g., alunite, ferric potassium alum, gypsum) and carbonate minerals (calcite, dolomite) can also be identified. Different degrees of mineral crystallinity cause infrared absorption peaks with different positions and shapes. The degree of crystallinity of a mineral indicates the temperature and chemical environment of hydrothermal alteration minerals during the mineralization process. Additionally, the degree of crystallinity of a mineral, to some extent, has something to do with the clay weathering of the mineral alteration system.

Spectral features relevant to mapping of alteration minerals can be detected in two wavelength regions. The first is visible and near infrared (VNIR) with a spectral scope from 400 to 1100 nm (usually via electronic processes), and the corresponding alteration minerals are related to ferric and ferrous oxides, silicates, sulfates and sulfides, and REEs; the second is shortwave infrared (SWIR) with a spectral range from 1100 to 2500 nm (vibrational processes), and the corresponding alteration minerals are carbonates and OH bearing minerals, such as clays, micas, chlorites, talc, epidote, amphiboles and sulfates. Based on different responses in the NIR and SWIR spectral ranges, a variety of minerals can be classified. Most of these alteration minerals show most diagnostic absorption features in the VNIR and SWIR spectral regions [5,49]. The main molecular bonds that cause absorption features in the spectral range from 1300 to 2500 nm for minerals and the corresponding main and secondary diagnostic absorption features are given in Table 2. The number of example minerals listed in Table 2 is limited because not all alteration minerals are active in the SWIR spectral region (and hence do not show diagnostic absorption features, and their

corresponding detailed absorption features are described in Figure 3). Once the spectral data have been obtained, according to the spectral matching method related to diagnostic spectral absorption features, it can be used to identify alteration zoning, changes in mineral proportions, mineral occurrence and mineral composition [50].

Table 2. Main molecular bonds related minerals with corresponding absorption features [51].

Molecular Bond	Absorption Feature (μm)	Example of Mineral of SWIR
Al-OH	2.160–2.220	Montmorillonite, Illite, Muscovite, Kaolinite
Mg-OH	2.300–2.360	Epidote, Chlorite, Antigorite
Carbonate (CO_3)	2.300–2.350	Calcite

Figure 3. Detailed absorption features of samples of minerals from the USGS mineral library that are listed in Table 2. (**a**) Minerals with Al-OH molecular bonds; (**b**) Minerals with Mg-OH and CO_3 molecular bonds.

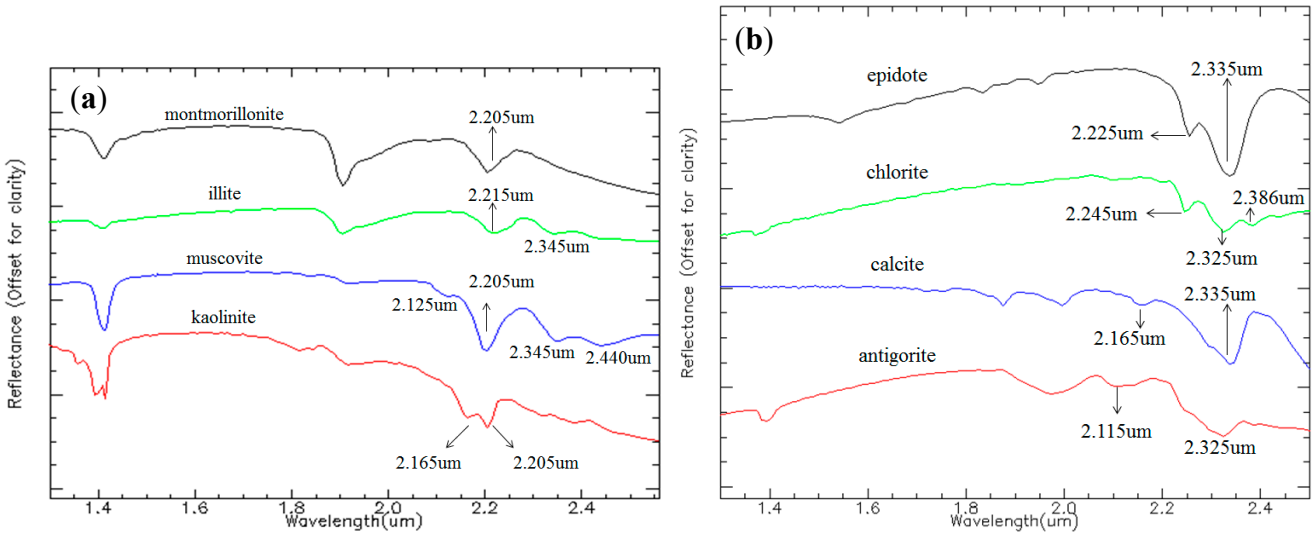

In Figure 3a the absorption features of muscovite, illite, kaolinite and montmorillonite are located in the vicinity of 2205 nm, 2215 nm, 2205 nm and 2205 nm, respectively. The secondary spectral absorption features of muscovite are located at 2125 nm, 2345 nm and 2440 nm. Illite's secondary diagnostic absorption feature is located at 2345 nm and kaolinite's secondary spectral absorption feature is located at 2165 nm. Figure 3b shows detailed spectral absorption features of minerals with Mg-OH bonds and carbonate (CO_3) bonds. As depicted in Figure 3a, the main diagnostic spectral absorption features of Al-OH molecular-bonding related minerals such as epidote, chlorite and antigorite are respectively located at 2335 nm, 2325 nm and 2325 nm, and the CO_3-related mineral calcite's main diagnostic spectral absorption feature is located at 2335 nm. The secondary diagnostic absorption feature of epidote is located at 2225 nm, chlorite's secondary diagnostic spectral absorption features are located at 2245 nm and 2386 nm, antigorite's secondary diagnostic spectral absorption feature is located at 2115 nm and calcite's secondary spectral absorption feature is located in the vicinity of 2165 nm.

4.2. Spectral Absorption Features and the SAI Model

The parameters characterizing the spectral absorption features are usually spectral absorption band-position, absorption band-width, absorption band-depth, absorption band-area, absorption band-slope, and the absorption band-symmetry (See Figure 4). The spectral characteristics of alteration minerals can be represented by these parameters. Throughout the analysis of the relationship between spectral absorption features and alteration minerals, it was found that the spectral absorption band-position was available and helpful for discriminating alteration minerals, whereas the spectral absorption band-depth could be used to retrieve the abundance and distribution of alteration minerals.

Figure 4. Spectral absorption features and SAI index model [24,41].

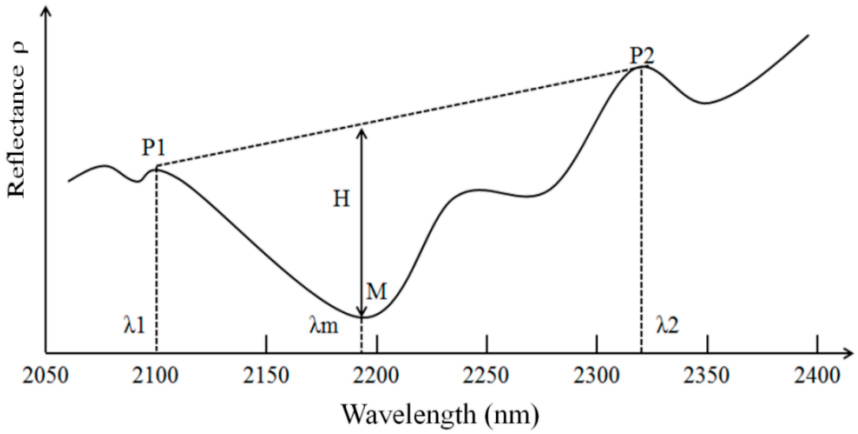

The detailed information of these parameters can be vividly depicted as in Figure 4. Therein, the absorption band-position is located at point M, which has the minimum value of spectral reflectance compared with the whole spectral region. The spectral absorption band-width W is the difference in wavelength between the two shoulders (point P_1 and P_2) of point M, and it can be expressed by the following equation:

$$W = \lambda_{p_2} - \lambda_{p_1} \tag{1}$$

where W is the spectral absorption band-width, P_1 and P_2 are the shoulders for point M, and λ is the wavelength. The symmetry can be defined as follows:

$$S = \frac{\lambda_{p_2} - \lambda_m}{W} \tag{2}$$

where S is the symmetry of the spectral absorption band, λ_m and λ_{p_2} are the respective wavelengths of points M and P_2, and W is the spectral absorption band-width.

The spectral absorption band-depth H is defined as the distance between point M and the non-absorption baseline, which passes through the two points P_1 and P_2. Before calculating the distance, we give an equation for the spectral reflectance difference as follows:

$$\Delta\rho = \rho_{p_1} - \rho_{p_2} \tag{3}$$

where $\Delta\rho$ is the spectral reflectance difference between points P_1 and P_2. Then, the non-absorption baseline is represented by the following equation:

$$W \cdot \rho - \Delta\rho \cdot \lambda = \rho_{p_1} - \Delta\rho \cdot \lambda_{p_1} \tag{4}$$

The distance H between point M and the non-absorption baseline can be calculated by the following equation:

$$H = \frac{\rho_2(\lambda_M - \lambda_1) - \rho_M(\lambda_2 - \lambda_M)}{\lambda_2 - \lambda_M} \quad (5)$$

where H is the above-mentioned distance, λ_i is the wavelength of each point, and ρ_i is the corresponding reflectance of each point.

Then, the spectral absorption index (SAI) is defined as the reciprocal of the ratio between the reflectance of point M and the corresponding value of the spectral absorption baseline, and it can be described by the following equation:

$$SAI = \frac{S\rho_{p_1} + (1 - S)\rho_{p_2}}{\rho_m} \quad (6)$$

where, SAI = spectral absorption index, S is the symmetry mentioned above, and ρ_{p_1}, ρ_{p_2}, and ρ_m is the corresponding reflectance of point P_1, P_2, and M.

5. Results

With the SAI model and on the basis of knowledge regarding spectral absorption features, using the interactive data language (IDL software, produced by ITT Co. Ltd., Boulder, CO, USA) to do coding of these absorption features, spectral absorption features relating to the main molecular bonds of Al-OH, Mg-OH and CO_3 were extracted from HyMap hyperspectral data of the study area (See Figures 5 and 6). With these results from the HyMap hyperspectral data, mapping of the corresponding alteration minerals was carried out (See Figure 7).

Figure 5. Alteration of mineral calcite extracted from HyMap data of the Gold-mine area. (**a**) is the spectral absorption index (SAI) image of calcite, (**b**) is the spectral absorption index (SAI) image of epidote, (**c**) is the spectral absorption index (SAI) image of muscovite, (**d**) is the spectral absorption index (SAI) image of antigorite.

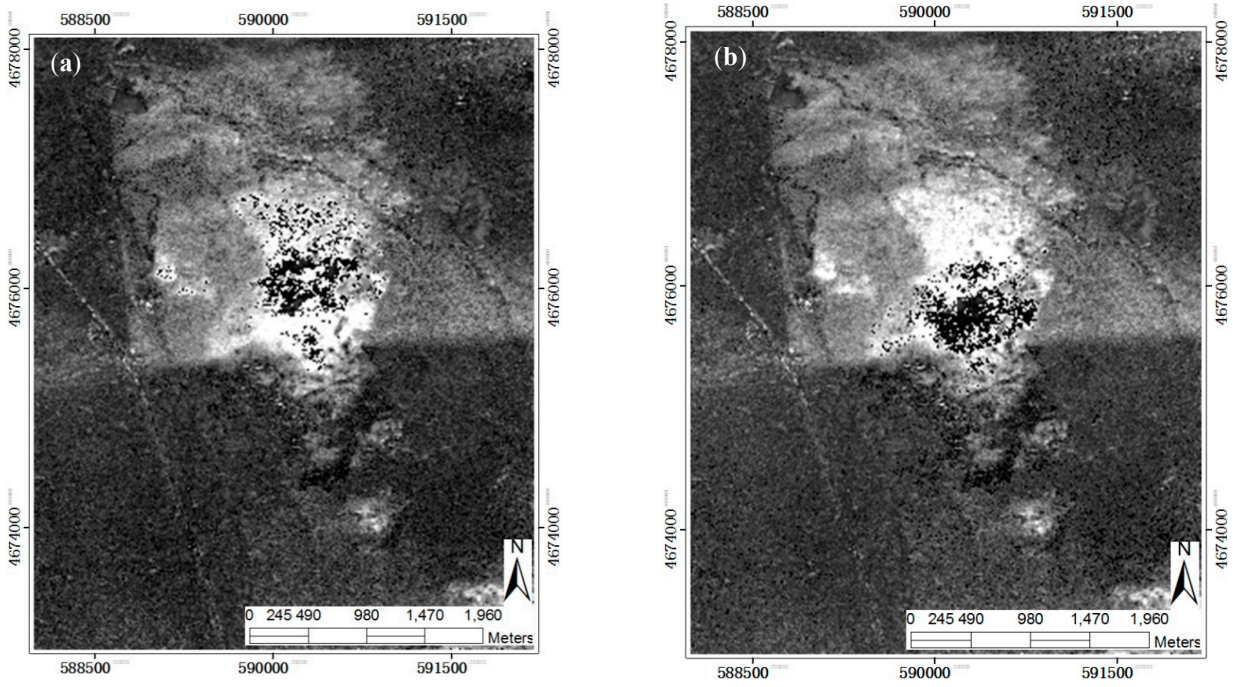

Figure 5. *Cont.*

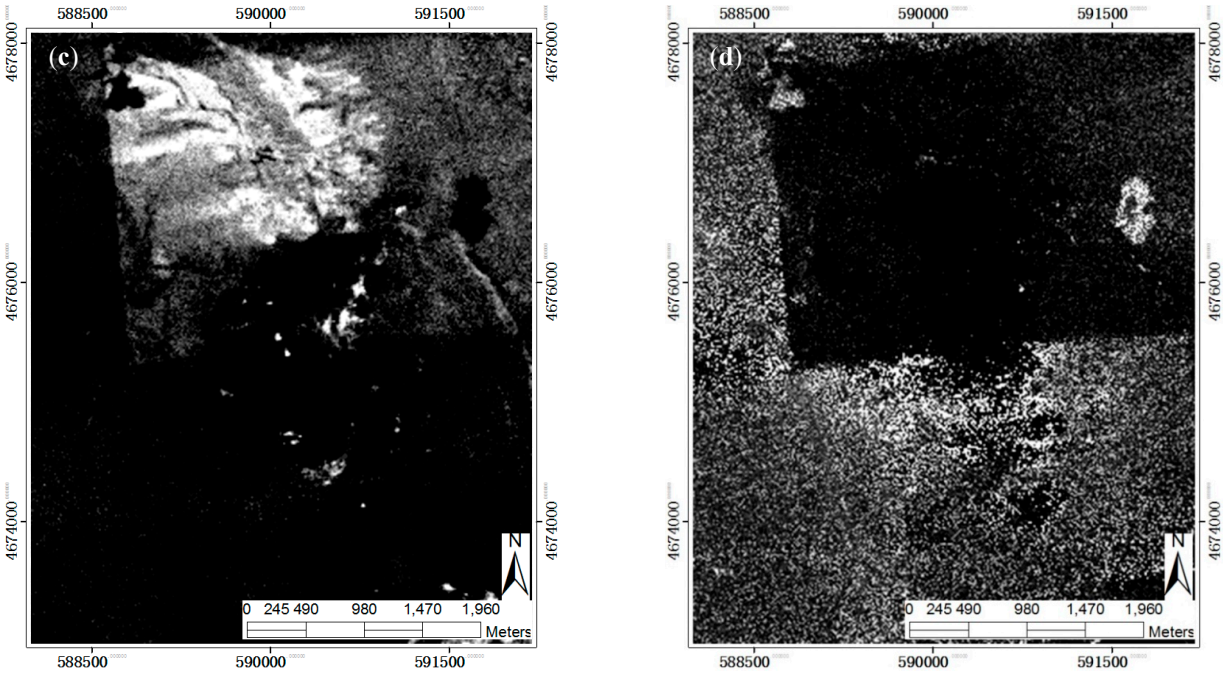

Figure 6. Alteration minerals by SAI extracted from HyMap data of Copper-mine area. (**a**) is the alteration mineral SAI image related to Al-poor muscovite, (**b**) is the alteration mineral SAI image related to Al-rich muscovite, (**c**) is the alteration mineral SAI related to antigorite information and (**d**) is the alteration mineral SAI image related to epidote information.

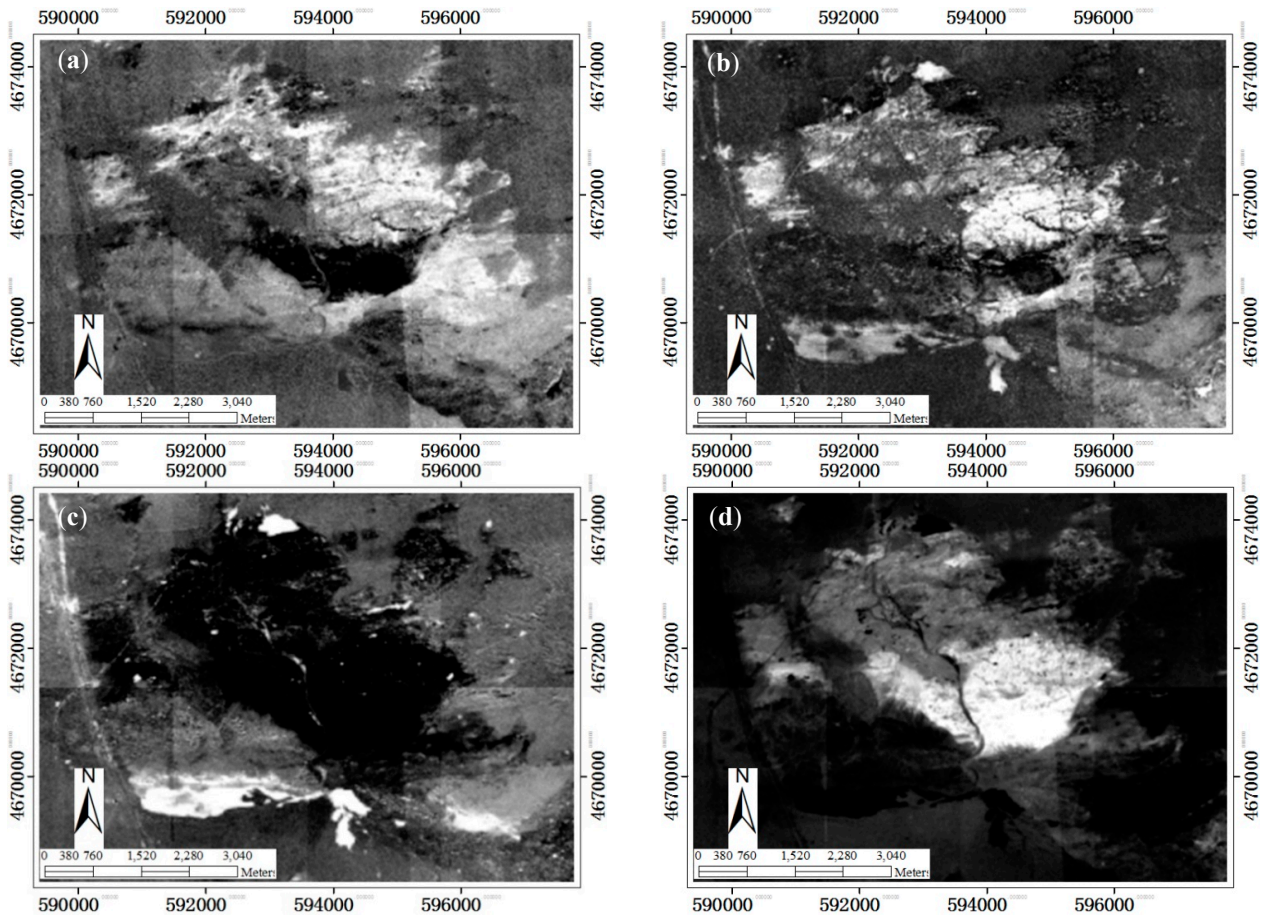

Figure 7. Mineral information extraction with the application of the SAI model and spectral absorption features from the HyMap data. (**a**) Mineral mapping of the gold-mine area (**b**) Mineral mapping of the copper-mine area.

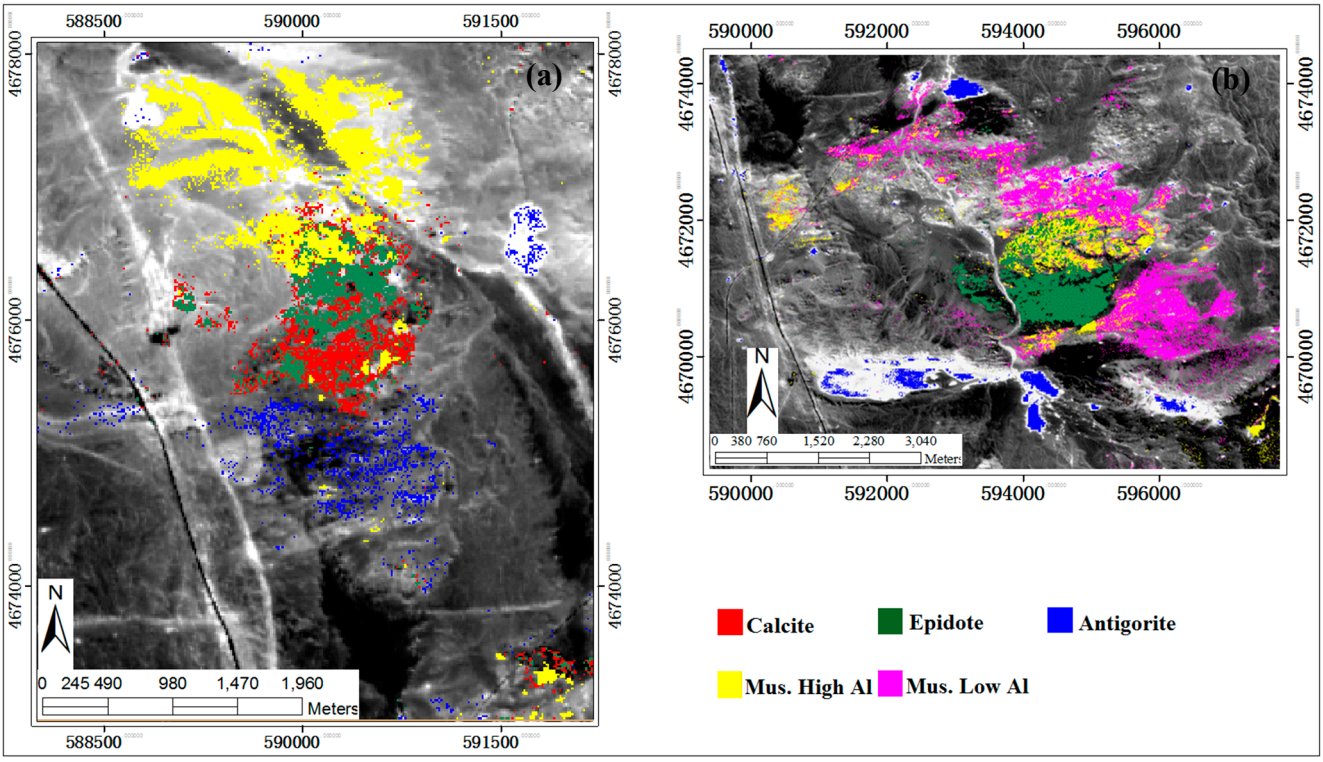

Mus. = Muscovite

Analysis of Alteration Mineral Information Extracted from Spectral Absorption Features

With knowledge of the minerals' spectra and their diagnostic spectral absorption features, the parameters mentioned in Section 4.2 and the corresponding SAIs were calculated from the HyMap data. According to the knowledge of mineral spectra, with the information extracted from the spectral absorption features, the major minerals related to the information were predicted and delineated, and they are listed in Table 3. In the table, the spectral absorption features used to distinguish Al-poor Muscovite from Al-rich Muscovite were available in only eastern Tien Shan, Xinjiang Uyghur Autonomous Region. In fact, the identification accuracy for Al-poor muscovite and Al-rich muscovite was less than 70% through the field survey. During the identification of alteration minerals, we found that it was difficult to distinguish epidote from calcite using only single bands as they have similar absorption features. Therefore, by combining the main absorption features listed in Table 3 with other secondary absorption features described in Figure 3, calcite could be distinguished from epidote and micas. Then, mineral mapping was carried out for the two study areas with the SAI model (See Figures 5 and 6).

Table 3. Detailed absorption feature information.

Band-Position (nm)	Absorption Shoulders (nm)	Band-Width (nm)	Band-Symmetry	Major Minerals Extracted
2330	* b104 = 2192 b115 = 2379	187	0.173	Calcite
2210	b103 = 2174 b108 = 2262	88	0.394	Al-poor Muscovite
2192	b102 = 2156 b110 = 2297	141	0.677	Al-rich Muscovite
2335	b109 = 2279 b119 = 2444	165	0.395	Epidote
2396	b114 = 2363 b120 = 2460	97	0.335	Antigorite

* bi is the band number of the HyMap data used in the study

Figure 5a is the resulting SAI image located in the vicinity of 2330 nm, namely b112 (band 112) and its two shoulders are b104 and b115. The mineral extracted from hyperspectral data was mainly calcite. Figures 5b and 6d are SAI images located in the vicinity of 2335 nm with shoulders located in the vicinity of 2279 nm and 2444 nm, and the main mineral information presented was epidote. Figures 5c and 6b are SAI images located in the vicinity of 2192 nm with shoulders in the vicinity of 2156 nm and 2297 nm, and the main mineral information extracted from the HyMap data was Al-rich muscovite. Figure 6a is an SAI image located in the vicinity of 2210 nm with shoulders at 2174 nm and 2262 nm, and the mineral information extracted from the airborne data mainly presented as Al-poor muscovite. 5d and 6c are SAI images located in the vicinity of 2396 nm with shoulders in the vicinity of 2363 nm and 2460 nm, and the main mineral extracted from the airborne data was antigorite.

6. Validation of Results Using Field Survey Based on Spectral Knowledge

To further validate and assess the accuracy of the results from spectral absorption features and SAI modeling, a field survey were carried out from 20 to 27 April 2010 with cloud-free days and a light wind, and during this season, the average atmospheric temperature is 15.2 °C. Before this job, the locations of sampling points were reasonably chosen on the basis of the results from the HyMap data, the results of previous literature and the alignment of gold ore veins and copper ore veins as the baseline combined with geological and terrestrial materials (see Figure 8). During the field survey, a total of 664 rock samples were collected, the number from the Copper mine area and Gold mine were 594 and 70, respectively. All the samples collected were prepared for processing using PIMA and the corresponding spectra were to be measured.

Measurement and Quantitative Analysis of Mineral Spectra in the Laboratory with a PIMA Spectrometer

Based on spectral knowledge combined with the advantages of the PIMA, the spectra of 594 rock samples were processed using the spectrometer. With the spectrum measurement work carried out in the laboratory, a total of 1226 spectra were measured using PIMA in the two regions of the study area,

among which 145 spectra of 70 samples collected in the gold-mine area were measured and 1081 spectra of 594 samples collected in the copper-mine area were measured.

Figure 8. Distribution of sampling point locations.

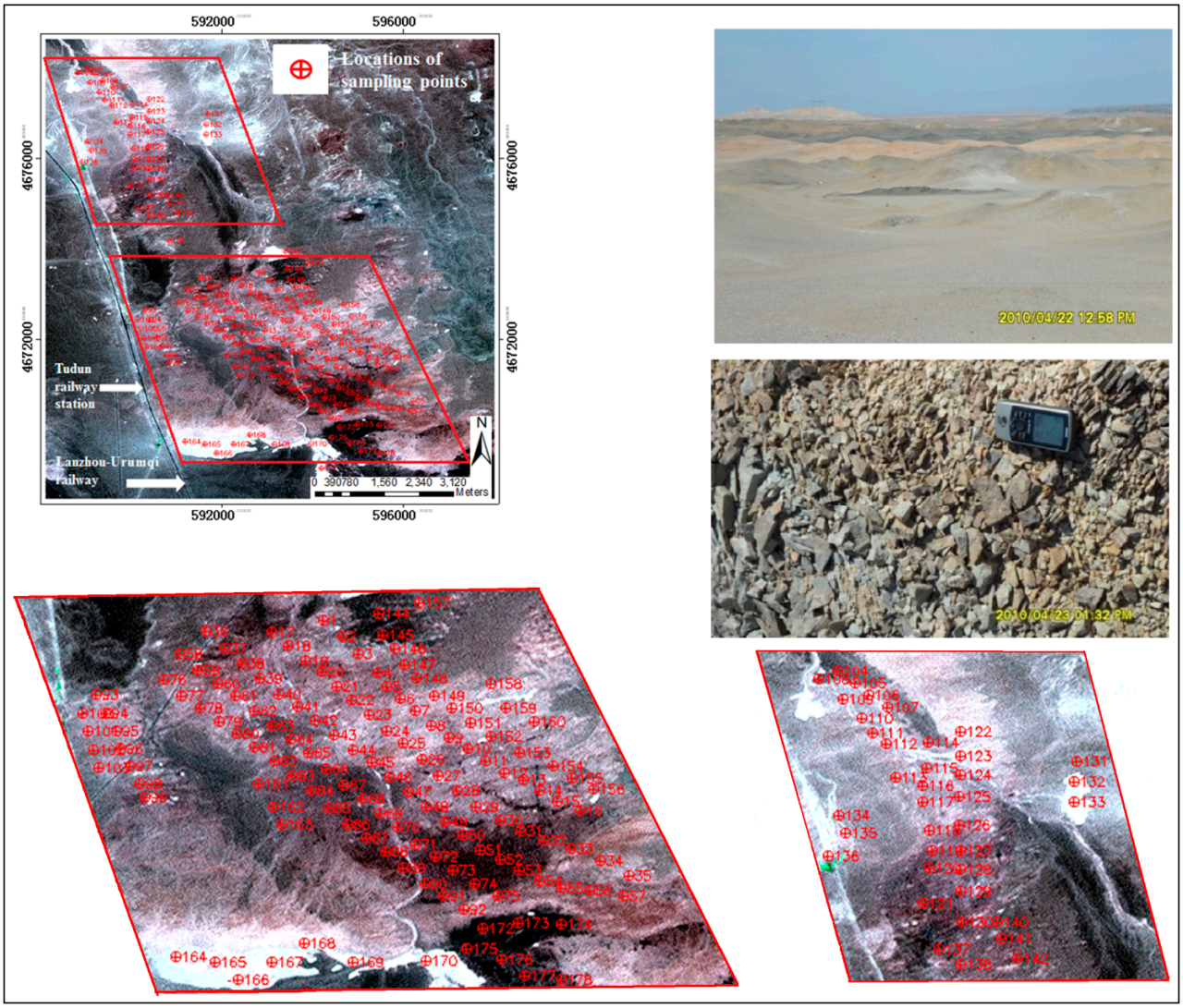

The spectra were interpreted using the spectral analyzing software infrared mineral spectrum measurement and analysis system (IMSMAS) affiliated with the PIMA. Using knowledge of the spectral absorption features, every rock sample was identified and discriminated with IMSMAS, and the relative abundance of the corresponding minerals was determined. A flowchart describing the quantitative analysis of the mineral spectra is shown in Figure 9.

During the process of quantitative analysis of the mineral spectra and quality control inspection, we found that 65 spectra of 31 samples were not identified, and we call them inefficient spectra. The remaining 1161 efficient spectra were processed and the results are summarized and listed in Table 4. Table 4 presents all the alteration minerals identified using PIMA, and the relative abundance of each mineral is described and classified into 6 levels including 15%–30%, 30%–45%, 45%–60%, 60%–75%, 75%–90%, and >90%. The number of spectra and samples of each percentage are listed in Table 4. Considering the accuracy of the PIMA and the impacts of environmental factors on the

measurements, we concluded that the relative abundance of one mineral being less than 15% had little effect on the whole spectra. Therefore, in the study, minerals with relative content below 15% were not counted and are not listed in Table 4. The spectra of the main minerals identified during the analysis are described in Figure 10. In the figure, pure spectra were presented to illustrate the validity of the PIMA data (to demonstrate that the PIMA spectra are similar to the USGS spectra).

Figure 9. Flowchart of mineral spectrum processing for quantitative analysis.

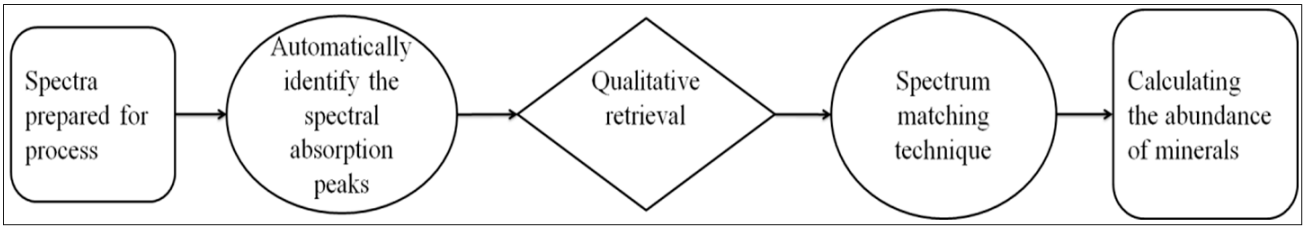

Table 4. Results of mineral identification and quantitative analysis obtained from the PIMA spectrometer.

Relative Amount (%) \ Mineral Components		Epidote	Chlorite	Muscovite	Illite	Calcite	Kaolinite	Quartz
15–30 (%)	**Number of Spectra**	120	51	136	21	11	14	45
	Number of Samples	105	43	107	19	10	13	41
31–45 (%)	**Number of Spectra**	89	31	62	21	9	8	23
	Number of Samples	81	28	55	19	9	8	22
46–60 (%)	**Number of Spectra**	77	11	50	23	7	8	41
	Number of Samples	70	10	48	18	7	8	39
61–75 (%)	**Number of Spectra**	131	5	57	17	7	4	41
	Number of Samples	116	4	50	13	7	4	39
76–90 (%)	**Number of Spectra**	172	1	36	12	18	5	36
	Number of Samples	148	1	31	12	16	5	33
>90 (%)	**Number of Spectra**	189	2	16	17	34	25	59
	Number of Samples	161	2	14	15	26	25	51
Total Spectra		778	101	357	111	99	64	245
Total Samples		681	88	305	96	75	63	225

From Table 4, according to the classified percentage of each mineral, we divided these minerals into three types including major minerals, secondary minerals and other components. The main minerals include epidote/chlorite alteration minerals, muscovite, illite alteration minerals, quartz, silica and calcite alteration minerals. The spectra of the main minerals were included in a comparative analysis with standard spectra from the USGS mineral library (see Figure 10), which showed a high degree of consistency. The main component of the secondary mineral was kaolinite. Other mineral components are at very low percentages (no more than 3%), which can be neglected. Considering the low amount of the secondary minerals and other mineral components, a comparative analysis between the testing spectra and the standard spectra of the USGS mineral library was not carried out in this study. The illite identified using PIMA is a common clay mineral, a hydrated mica that shares with other Al-clays (*i.e.*, smectite and kaolin group) the AlOH feature located at approximately 2200 nm. The mineral illite

has a property of being rich in potassium and aluminum but poor in iron. In this study, the illite identified using PIMA was regarded as Al-rich muscovite extracted from HyMap data on the basis of SAI modeling. In addition, observation of these major minerals' spectra revealed that illite was often accompanied by alteration minerals, such as kaolinite, muscovite, epidote and chlorite. In general, through the validation of the HyMap data results with the field survey and the test spectra measured using PIMA, the results of mineral mapping from HyMap data have a very high degree of consistency with the field survey.

Figure 10. Comparative analysis between the spectra of the main minerals identified in the study and the USGS mineral library. The main minerals identified using the spectrometer are (**a**) epidote, (**b**) quartz, (**c**) illite, (**d**) calcite, (**e**) muscovite and (**f**) chlorite.

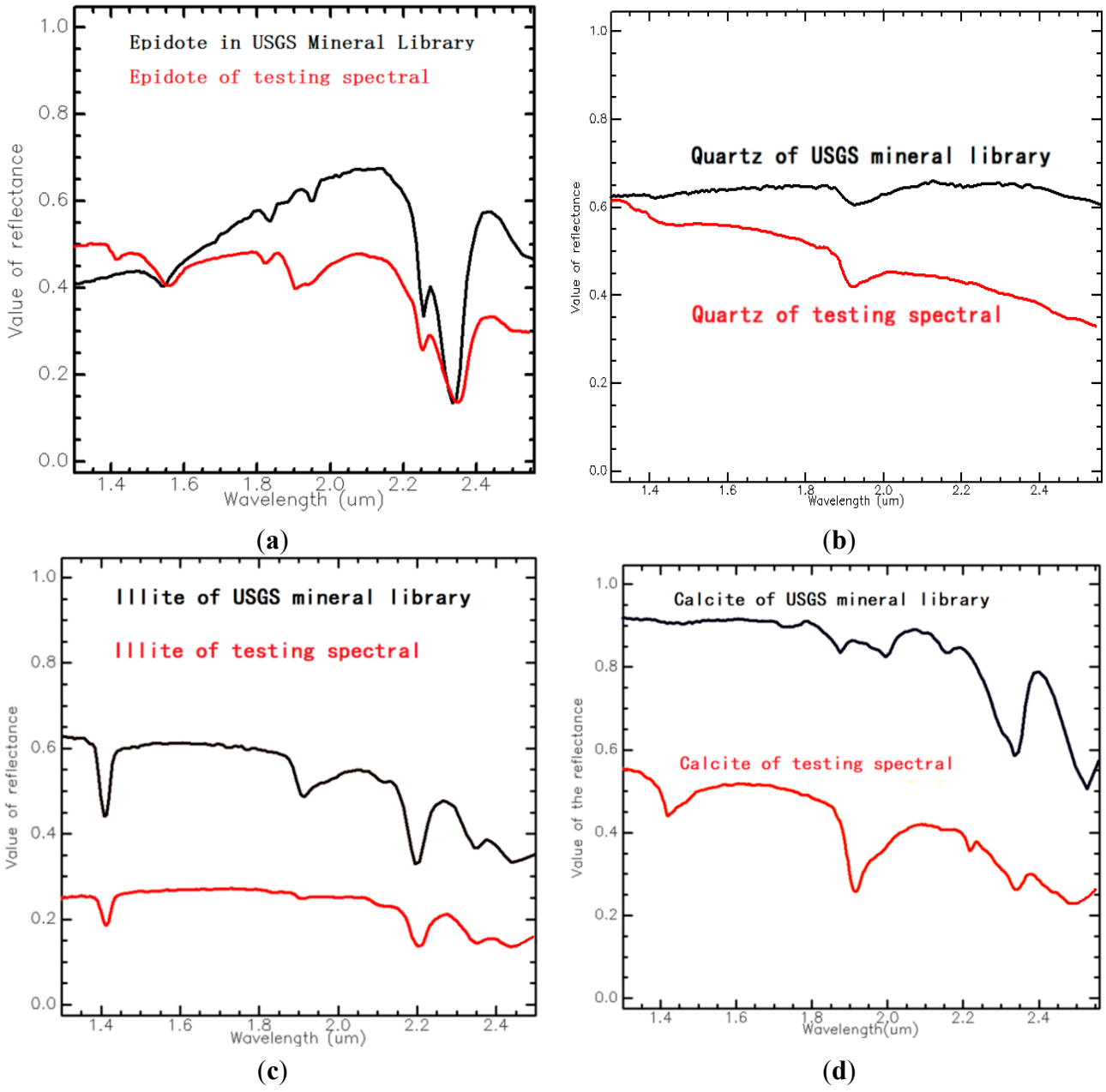

Figure 10. *Cont.*

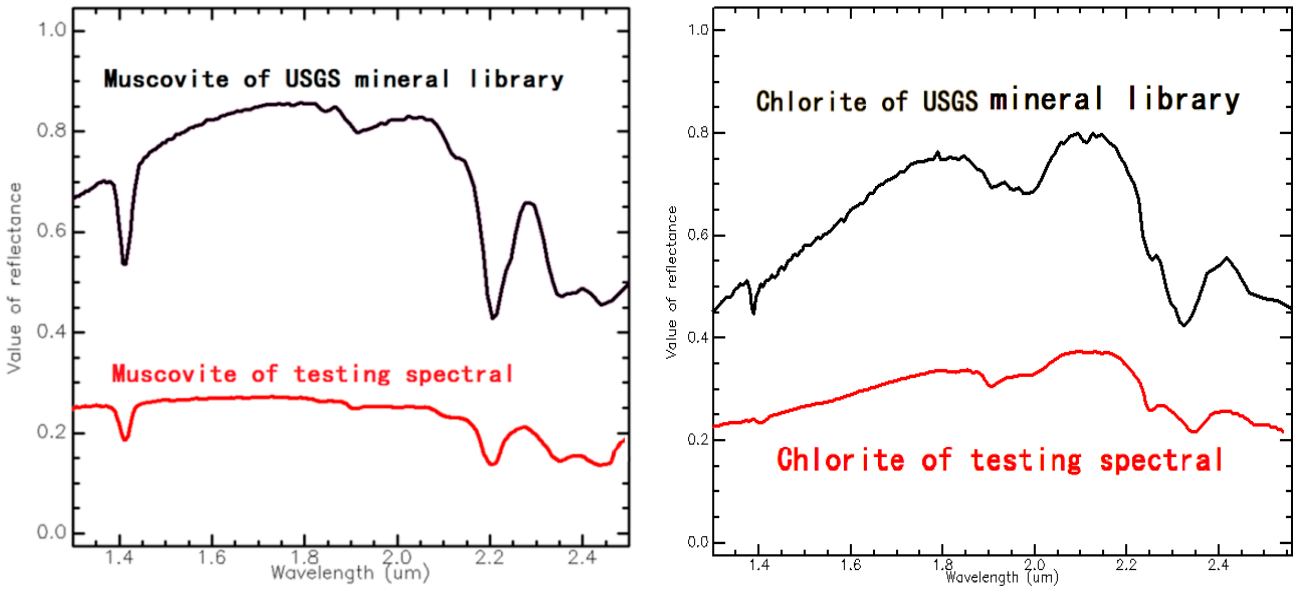

(e) **(f)**

To find the relationship between mineral abundance and these spectral absorption features, a comparative analysis was conducted and the absorption features of the several main minerals based on the model mentioned in Section 4.2 were calculated, and the detailed information is presented in Figure 11. In the figure, considering that the secondary minerals and other rare components play an unimportant and inconspicuous role in all the categories of minerals identified using PIMA, and taking the limited spectrum of calcite into account, only four main minerals, including muscovite, epidote, quartz and illite, were described. The figure shows that the SAI and the spectral absorption band-depth correlate well with one another and with the variation of relative alteration mineral abundance (the values of the SAI and the spectral absorption band-depth decrease with the corresponding reduction of relative alteration mineral abundance), whereas there was no obvious positive relationship between the spectral absorption band-symmetry and the abundance of alteration minerals.

7. Ore Prospecting

The study area is located at the conjunction of Tarim plate and the Junggar Plate, which is a part of the Tage Kangguer Devonian and Carbo island arc belt in the southeast margin of the Junggar plate of the Jueluotage Carboniferous island arc in the active leading edge of the Tarim plate, and the deposits in an outcrop of Middle Carboniferous Series Wutongyaozi Formation (C2wd) are light-red/gray felsic porphyry, dark green/light gray diabase and carbonaceous shale/metamorphic siltstone. The rock mass in the study area is granite and diorite from the Middle Variscan period. Metamorphism in the area is mainly dynamic metamorphism and hydrothermal metamorphism related to structural fracturing and hydrothermal alteration. The formation of dynamic metamorphism in the area is mainly accompanied with fault structures, and the corresponding distribution shows a zonal shape along the tectonic line. The formation of hydrothermal metamorphism is located in the fault structure belt and interlayer fracture, and the corresponding magnitude and intensity depends on the structure's scale and properties.

Figure 11. Statistics of spectral absorption features of alteration minerals identified using PIMA and the relationship between the spectral absorption features (including SAI, spectral absorption band-depth, spectral absorption band-width, spectral absorption band-symmetry and spectral absorption composition) and the relative abundance of alteration minerals.

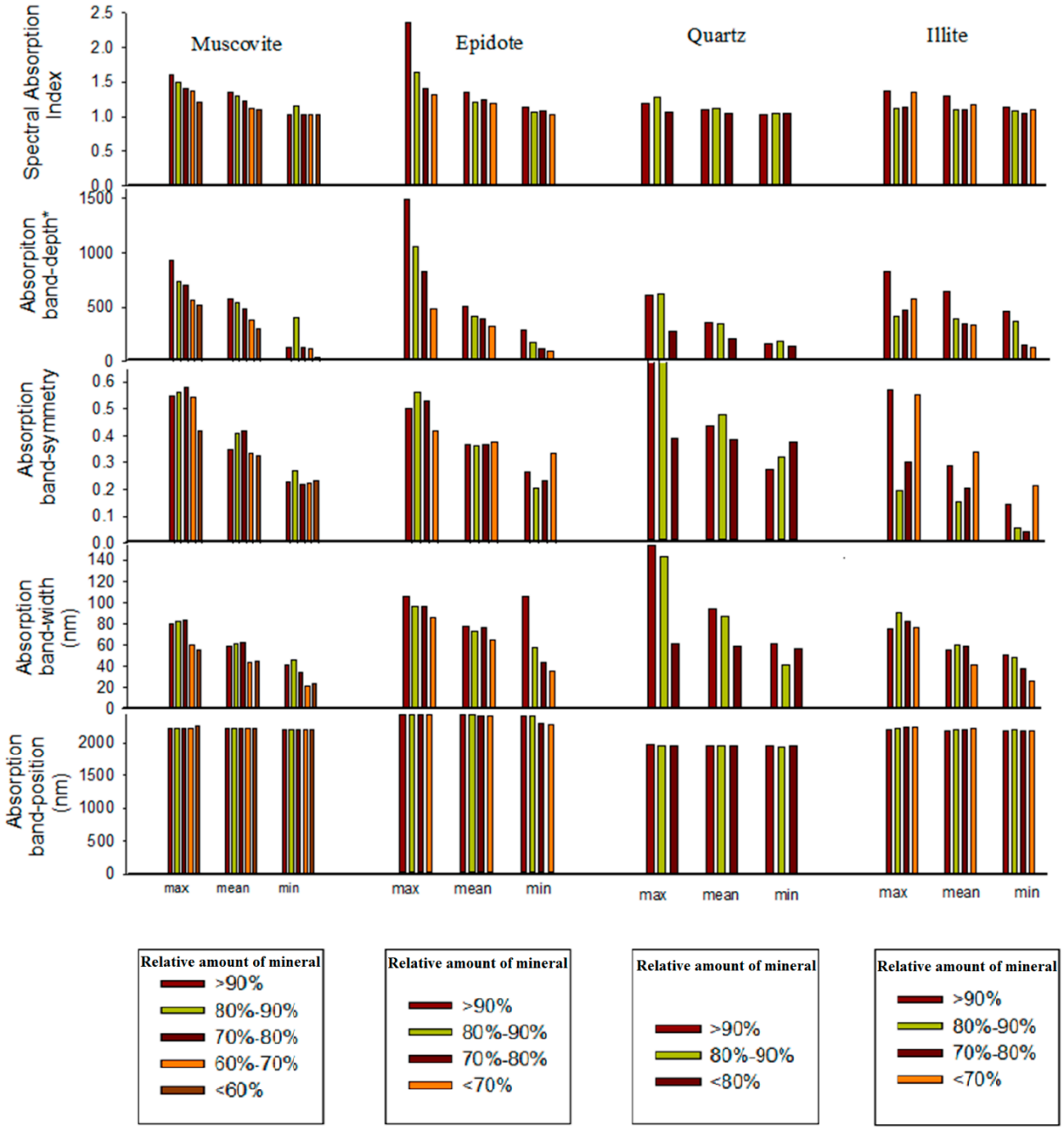

* Scaling factor = 1000

In the Gold-mine area, the hydrothermal alteration mainly produced epidote, muscovite, calcite and antigorite alterations, which were extracted from the HyMap data. From Figure 7 showing the mineral alteration distribution and the field survey carried out from April 20 to 27 in 2010, we found that most of the epidote and calcite minerals appeared in a wide range of block distribution, and the two minerals

had a close spatial relationship and simultaneously existed in some areas of the study area. In the northern and northwestern part of the distribution area of the two above-mentioned minerals, there was mineralized muscovite alteration showing a sheet or block distribution. In addition, the distribution of antigorite extracted from the HyMap data is more fragmented and scattered, occurring mainly in the southern part of the distribution area of epidote and calcite.

In the Copper-mine area, the main minerals extracted from the HyMap data included epidote, Al-poor muscovite, Al-rich muscovite and small amounts of antigorite and kaolinite. The Al-poor muscovite with a sheet distribution is distributed in the north and northeast region of the copper-mine area, and the Al-rich muscovite shows a block distribution enclosed by the distribution area of Al-poor muscovite. The epidote/chlorite mineral alterations were distributed in the south of the copper area, the area of which was surrounded by scattered antigorite. From Figure 8, we found that muscovite, epidote and chlorite show spatial overlap and intersecting zone demonstrating a close spatial relationship between muscovite and epidote/chlorite.

In general, in the Gold-mine area in the north of the study area, the cause of muscovite, calcite and epidote mineral alteration, had a direct and close relationship with that of granite and diorite, and the close spatial relationship among these three mineral alterations predicted better prospecting for gold ore in the area. In the Copper-mine area in the southern part of the study area, the spatial distribution and relationship of the Al-poor muscovite, Al-rich muscovite, epidote and chlorite mineral alterations predicted this region as a better area for prospecting copper ore.

8. Conclusions

In the study, mineral alterations, such as epidote, calcite, Al-poor muscovite, Al-rich muscovite and antigorite were identified based on the SAI model and spectral absorption features using HyMap hyperspectral data. A comparative analysis was performed with previous literature results to show the quality of the mineral mapping results based on HyMap data, and it revealed a high degree of consistence with the previous literature. To further validate the results of the mineral mapping from HyMap images, a field survey was carried out and rock samples were collected from 20 to 27 April 2010 for further laboratory spectral analysis. During the field survey, we found that the results had a good degree of consistence with the local geology. In the laboratory work, the spectra of rock samples were processed using a PIMA. Quantitative analyses of the rock samples' spectra and the relative abundance of alteration minerals were determined using the IMSMAS. Based on the SAI and other spectral absorption features, the relationship between these spectral absorption features and the relative abundance of minerals was analyzed. The results showed that the spectral absorption band-depth and the SAI had a higher degree of consistency with the relative abundance of minerals than the other spectral absorption features, in particular the spectral absorption band-depth provides a better representation. Then, the ore prospecting potential of the study area was predicted in the paper. The distribution and close spatial relationship among the minerals extracted from the HyMap data showed good ore prospecting potential for the Gold-mine area and the Copper-mine area.

Through the cross-validation, the field survey and the spectral analysis with IMSMAS, we concluded that the SAI model and the spectral absorption features showed high accuracy and precision in mineral identification and mineral mapping because the model could reduce the influence of solar radiance

variation. However, there is a problem that needs to be resolved. Before quantitative analysis with the SAI model and spectral absorption feature calculation equations, the reflectance spectra of the HyMap data should be reconstructed on the basis of rigorous calibration and both atmospheric and geometric correction.

The SAI model on the basis of spectral absorption features has universal significance. It can be widely used for mineral identification and quantitative analysis. The premise before using the model is that these spectral absorption features should be calculated and consummated. In addition, the SAI model can be characterized as a function of single scattering albedo so it can be used to map the abundance of mineral alterations, but the precision and accuracy should be improved in a further step. Another problem occurred during the mineral identification process: although the SAI model puts the emphasis on single spectral absorption features, in practical geological applications, it is difficult to distinguish and classify those minerals that have similar spectral absorption features such as epidote and chlorite.

Acknowledgements

This work is supported by the National Science and Technology Major Project (2011ZX05039-004), by the National High Technology Research and Development Program of China (2012AA12A204), and by the National Natural Science Foundation of China (41231170), and by the National Natural Science Foundation of China (41471297).

Author Contributions

All authors contributed equally to this work. Xiaoguang Jiang supervised the project. Hongyuan Huo and Zhuoya Ni performed the field survey and validated the results with the field survey data. Zhuoya Ni and Liang Liu performed the satellite datasets preprocessing. Hongyuan Huo performed analysis of the results with the programs developed by Zhuoya Ni and Liang Liu. Hongyuan Huo wrote the paper. Ping Zhou gave a lot of valuable advice during the process of revision of this paper. All authors discussed the results and implications and commented on the manuscript at all stages.

Conflicts of Interest

The authors declare no conflict of interest.

References

1. Duke, E.F. Near infrared spectra of muscovite, Tschermak substitution, and metamorphic reaction progress: implications for remote sensing. *Geology* **1994**, *22*, 621–624.
2. Green, R.O.; Eastwood, M.L.; Sarture, C.M.; Chrien, T.G.; Aronsson, M.; Chippendale, B.J.; Faust, J.A.; Pavri, B.E.; Chovit, C.J.; Solis, M.; *et al.* Imaging spectroscopy and the airborne visible/infrared imaging spectrometer (AVIRIS). *Remote Sens. Environ.* **1998**, *65*, 227–248.
3. Hubbard, B.E.; Crowley, J.K.; Zimbelman, D.R. Comparative alteration mineral mapping using visible to shortwave infrared (0.4–2.4 μm) Hyperion, ALI, and ASTER imagery. *IEEE Trans. Geosci. Remote Sens.* **2003**, *41*, 1401–1410.

4. Velasco, F.; Alvaro, A.; Suarez, S.; Herrero, J.M.; Yusta, I. Mapping Fe-bearing hydrated sulphate minerals with short wave infrared (SWIR) spectral analysis at San Miguel mine environment, Iberian Pyrite Belt (SW Spain). *J. Geochem. Explor.* **2005**, *87*, 45–72.
5. Petrovic, A.; Khan, S.D.; Thurmond, A.K. Integrated hyperspectral remote sensing, geochemical and isotopic studies for understanding hydrocarbon-induced rock alterations *Mar. Petrol. Geol.* **2012**, *35*, 292–308.
6. Kruse, F.A.; Perry, S.L. Mineral mapping using simulated Worldview-3 short-wave-infrared imagery. *Remote Sens.* **2013**, *5*, 2688–2703.
7. Haest, M.; Cudahy, T.; Laukamp, C.; Gregory, S. Quantitative mineralogy from visible to shortwave infrared spectroscopic data: (II) 3D mineralogical characterisation of the Rocklea Dome channel iron deposit in Western Australia. *Econ. Geol.* **2012**, *107*, 229–249.
8. Haest, M.; Cudahy, C.; Rodger, A.; Laukamp, C.; Martens, E.; Caccetta, M. Unmixing vegetation from airborne visible-near to shortwave infrared spectroscopy-based mineral maps over the Rocklea Dome (Western Australia), with a focus on iron rich palaeochannels. *Remote Sens. Environ.* **2013**, *129*, 17–31.
9. Crowley, J.K.; Hook, S.J. Mapping playa evaporite minerals and associated sediments in Death Valley, California, with multispectral thermal infrared images. *J. Geophys. Res.* **1996**, *101*, 643–660.
10. Yamaguchi, Y.; Kahle, A.B.; Tsu, H.; Kawakami, T.; Pniel, M.. Overview of advanced spaceborne thermal emission and reflection radiometer (ASTER). *IEEE Trans. Geosci. Remote Sens.* **1998**, *36*, 1062–1071.
11. Li, Z.-L.; Becker, F.; Stoll, M.P.; Wan, Z. Evaluation of six methods for extracting relative emissivity spectral from thermal infrared images. *Remote Sens. Environ.* **1999**, 69, 197–214.
12. Vaughan, R.G.; Hook, S.J.; Calvin, W.M.; Taranik, J.V. Surface mineral mapping at Steamboat Springs, Nevada, USA, with multi-wavelength thermal infrared images. *Remote Sens. Environ.* **2005**, *99*, 140–158.
13. Hecker, C.; Van der Meijde, M.; Van der Meer, F.D. Thermal infrared spectroscopy on feldspars—Successes, limitations and their implications for remote sensing. *Earth-Sci. Rev.* **2010**, *103*, 60–70.
14. Becker, F.; Li, Z.-L. Temperature independent spectral indices in thermal infrared bands. *Remote Sens. Environ.* **1990**, *32*, 17–33.
15. Li, Z.-L.; Becker, F. Properties and comparison of temperature independent thermal infrared spectral indices with NDVI for HAPEX data. *Remote Sens. Environ.* **1990**, *33*,165–182.
16. Casey, K.A.; Kääb, A.; Benn, D.I. Geochemical characterization of supraglacial debris via *in situ* and optical remote sensing methods: A case study in Khumbu Himalaya, Nepal. *The Cryosphere* **2012**, *6*, 85–100.
17. Li, Z.-L.; Wu, H.; Wang, N.; Qiu, S.; Sobrino, J.A.; Wan, Z.; Tang, B.-H.; Yan, G.J. Land surface emissivity retrieval from satellite data. *Int. J. Remote Sens.* **2013**, *34*, 3084–3127.
18. Li, Z.-L., Tang, B.-H.; Wu, H.; Ren, H.; Yan, G.J.; Wan, Z.; Trigo, I.F.; Sobrino, J. Satellite-derived land surface temperature: Current status and perspectives. *Remote Sens. Environ.* **2013**, *131*, 14–37.
19. Riley, D.N.; Hecker, C.A. Mineral mapping with airborne hyperspectral thermal infrared remote sensing at Cuprite, Nevada, USA. *Therm. Infrared Remote Sens.* **2013**, *17*, 495–514.

20. da Silva, A.Q.; Paradella, W.R.; Freitas, C.C.; Oliveira, C.G. Evaluation of digital classification of polarimetric SAR data for iron-mineralized laterites mapping in the Amazon Region. *Remote Sens.* **2013**, *5*, 3101–3122.
21. Ni, Z.Y; Huo, H.Y.; Gan, F.P.; Wang, Y.Q.; Li, X.W.; Liu, Z.G. Lithological discrimination based on the inversion of roughness in Hami Area, Xinjiang. *IOP Conf. Ser.: Earth Environ. Sci.* **2014**, doi:10.1088/1755-1315/17/1/012274.
22. Wang, Q.H.; Wang, R.S.; Guo, X.F. Application for discrimination of rock using hyperspectral remote sensing technique. *Remote Sens. Land Resour.* **2000**, *4*, 7.
23. Laukamp, C.; Cudahy, T.; Caccetta, M.; Chia, J.; Gessner, K.; Haest, M.; Liu, Y.C.; Rodger, A. The uses, abuses and opportunities for hyperspectral technologies and derived geoscience information. *Hyperspectral Technol. Deriv. Geosci. Inf.* **2010**, *51*, 73–76.
24. Laukamp, C.; Cudahy, T.; Thomas, M.; Jones, M.; Cleverley, J.; Oliver, N. Hydrothermal mineral alteration patterns in the Mount Isa Inlier revealed by airborne hyperspectral data. *Aust. J. Earth Sci.* **2011**, *58*, 917–936.
25. Laukamp, C.; Cudahy, T.; Cleverley, J.; Oliver, N.; Hewson, R. Airborne hyperspectral imaging of hydrothermal alteration zones in granitoids of the Eastern Fold Belt, Mount Isa Inlier, Australia. *Geochem. Explor. Environ. Anal*. **2011**, *11*, 3–24.
26. Rodger, A. SODA: A new method of in-scene atmospheric water vapor estimation and post-flight spectral recalibration for hyperspectral sensors: Application to the HyMap sensor at two locations. *Remote Sens. Environ.* **2011**, *115*, 536–547.
27. Rogge, D.; Rivard, B.; Segl, K.; Grant, B.; Feng, J. Mapping of NiCu–PGE ore hosting ultramafic rocks using airborne and simulated EnMAP hyperspectral imagery, Nunavik, Canada. *Remote Sens. Environ.* **2014**, *152*, 302–317.
28. Gan, F.; Wang, R.; Ma, A. Spectral identification tree (SIT) for mineral extraction based on spectral characteristics of minerals. *Earth Sci. Front.* **2003**, *10*, 445–454.
29. Wang, R. Spectral identification and inversion of composition and component of objects with hyperspectral remote sensing. *J. GeoInf. Sci.* **2009**, *11*, 261–267.
30. Fenstermaker, L.K.; Miller, J.R. Identification of fluvially redistributed mill tailings using high spectral resolution aircraft data. *Photogramm. Eng. Remote Sens.* **1994**, *60*, 989–995.
31. Yuhas, R.H.; Goetz, A.F.; Boardman, J.W. Discrimination among semi-arid landscape endmembers using the spectral angle mapper (SAM) algorithm. In Proceedings of 1992 Summaries of the Third Annual JPL Airborne Geoscience Workshop, Pasadena, CA, USA, 1–5 June 1992; pp. 147–149.
32. De Carvalho, O., Jr.; Meneses, P. Spectral correlation mapper (SCM): An improvement on the spectral angle mapper (SAM). In Proceedings of 2000 Summaries of the 9th Airborne Earth Science Workshop, Pasadena, CA, USA, 23–25 Februray 2000; pp.65–74.
33. Chang, C.-I. An information-theoretic approach to spectral variability, similarity, and discrimination for hyperspectral image analysis. *IEEE Trans. Inform. Theory* **2000**, *46*, 1927–1932.
34. Du, H.; Qi, H.; Peterson, G.D. Parallel ica and its hardware implementation in hyperspectral image analysis. *Int. Soc. Opt. Photonics* **2004**, doi:10.1117/12.543962.
35. Van der Meer, F. The effectiveness of spectral similarity measures for the analysis of hyperspectral imagery. *Int. J. Appl. Earth Obs. Geoinf.* **2006**, *8*, 3–17.

36. Van der Meer, F.; Bakker, W.; CCSM: Cross correlogram spectral matching. *Int. J. Remote Sens.* **1997**, *18*, 1197–1201.
37. Clark, R.N.; Gallagher, A.J.; Swayze, G.A. Material absorption band depth mapping of imaging spectrometer data using a complete band shape least-squares fit with library reference spectra. In Proceedings of 1990 the Second Airborne Visible/Infrared Imaging Spectrometer (AVIRIS) Workshop, Denver, CO, USA, 4–5 July 1990; pp. 4–5.
38. Abílio, O.; Júnior, C.; Meneses, P. R.; Guimarães, R.F. Analysis absorption band positioning: A new method for hyperspectral image treatment. In Proceedings of 2001 AVIRIS Workshops, Pasadena, CA, USA, 27 February–2 March 2001; pp. 59–65.
39. Wang, J.-N.; Zheng, L.-F.; Tong, Q.-X. The spectral absorption identification model and mineral mapping by imaging spectrometer data. *J. Remote Sens.* **1996**, *11*, 20–31. (In Chinese)
40. Rodger, A.; Laukamp, C.; Haest, M.; Cudahy, T. A simple quadratic method of wavelength tracking for absorption features in continuum removed spectra. *Remote Sens. Environ.* **2012**, *118*, 273–283.
41. Van Ruitenbeek, F.J.A.; Debba, P.; Van der Meer, F.D.; Cudahy, T.; Van der Meijde, M.; Hale, M. Mapping white micas and their absorption wavelengths using hyperspectral band ratios. *Remote Sens. Environ.* **2006**, *102*, 211–222.
42. Gabr, S.; Ghulam, A.; Kusky, T. Detecting areas of high-potential gold mineralization using ASTER data. *Ore Geol. Rev.* **2010**, *38*, 59–69.
43. Ranjendran, S.; Al-Khirbash, S., Pracejus, B.; Nasir, S.; Al-Abri, A.H.; Kusky, T.M.; Ghulam, A. ASTER detection of chromite bearing mineralized zones in Semail Ophiolite Massifs of the northern Oman Mountains: Exploration strategy. *Ore Geol. Rev.* **2012**, *44*, 121–135.
44. Rajendran, S.; Nasir, S.; Kusky, T.M.; Ghulam, A.; Gabr, S.; Gali, M.E. Detection of hydrothermal mineralized zones associated with Listwaenites rocks in the Central Oman using ASTER data. *Ore Geol. Rev.* **2013**, *53*, 470–488.
45. Liu, L.; Zhou, J.; Jiang, D.; Zhuang, D.; Mansaray, L.R.; Zhang, B. Mansaray; Bing Zhang. Targeting mineral resources with remote sensing and field data in the Xiemisitai area, West Junggar, Xinjiang, China. *Remote Sens.* **2013**, *5*, 3156–3171.
46. Wang, R.; Liu, D.; Yin, D. Research over the copper and nickel sulfide deposits metallogenic control conditions and the ore prospecting in the area of Tudun-Huangshan mountain in Hami, Xinjiang Uyghur Autonomous Region. *J. Mineral. Petrol*. **1987**, *7*, 1–152. (In Chinese)
47. Yong, W. Study over the characteristic of the basic-ultrabased rock and the ability of containing ore, in Tudun area, Hami City, Xinjiang Uyghur Autonomous Region. *Xinjiang Nonferrous Metals* 2002, *25*, 1–6. (In Chinese)
48. Cocks, T.; Jenssen, R.; Stewart, A.; Wilson, I.; Shields, T. The HyMap airborne hyperspectral sensor: The system, calibration and performance. In Proceedings of 1998 EARSeL Workshop on Imaging Spectroscopy, Zurich, Sweden, 6–8 October 1998; pp. 37–43.
49. Notesco, G.; Kopačková, V.; Rojík, P.; Schwartz, G.; Livne, I.; Dor, E.B. Mineral classification of land surface using multispectral LWIR and hyperspectral SWIR remote-sensing data. A case study over the Sokolov lignite open-pit mines, the Czech Republic. *Remote Sens.* **2014**, *6*, 7005–7025.

50. Martin, Gabriel, and Antonio Plaza. Spatial-spectral preprocessing prior to end member identification and un-mixing of remotely sensed hyperspectral data. *IEEE J. Sel. Top. Appl. Earth Obs. Remote Sens.* **2012**, *5*, 380–395.
51. Robben, M.R. NIR Sensor Sorting, Basic study for application of NIR spectroscopy for sorting minerals. Bachelor's Thesis, Rheinisch-Westfälische Technische Hochschule Aachen, Aachen, Germany, 2008